Quantum memory with millisecond coherence in circuit QED

Matthew Reagor, Wolfgang Pfaff, Christopher Axline, Reinier W. Heeres, Nissim Ofek, Katrina Sliwa, Eric Holland, Chen Wang, Jacob Blumoff, Kevin Chou, Michael J. Hatridge, Luigi Frunzio, Michel H. Devoret, Liang Jiang, and Robert J. Schoelkopf

Phys. Rev. B **94**, 014506 — Published 8 July 2016

DOI: 10.1103/PhysRevB.94.014506

A quantum memory with millisecond coherence times in circuit QED

Matthew Reagor,[1,*] Wolfgang Pfaff,[1] Christopher Axline,[1] Reinier W. Heeres,[1] Nissim Ofek,[1] Katrina Sliwa,[1] Eric Holland,[1] Chen Wang,[1] Jacob Blumoff,[1] Kevin Chou,[1] Michael J. Hatridge,[1] Luigi Frunzio,[1] Michel H. Devoret,[1] Liang Jiang,[1] and Robert J. Schoelkopf[1]

[1] *Departments of Applied Physics and Physics, Yale University, New Haven, CT 06520, USA*

(Dated: June 6, 2016)

Significant advances in coherence render superconducting quantum circuits a viable platform for fault-tolerant quantum computing. To further extend capabilities, highly coherent quantum systems could act as quantum memories for these circuits. A useful quantum memory must be rapidly addressable by Josephson junction-based artificial atoms, while maintaining superior coherence. We demonstrate a novel superconducting microwave cavity architecture that is highly robust against major sources of loss that are encountered in the engineering of circuit QED systems. The architecture allows for storage of quantum superpositions in a resonator on the millisecond scale, while strong coupling between the resonator and a transmon qubit enables control, encoding, and readout at MHz rates. This extends the maximum available coherence time attainable in superconducting circuits by almost an order of magnitude compared to earlier hardware. Our design is an ideal platform for studying coherent quantum optics and marks an important step towards hardware-efficient quantum computing in Josephson junction-based quantum circuits.

I. INTRODUCTION

The ongoing quest to build a quantum computer demands continually improving the coherence of quantum states while scaling up the system size. Superconducting quantum circuits have experienced enormous improvements in coherence over the last decade, making them a leading contender for the implementation of practical quantum information processing devices. To date, quantum states encoded in such circuits can reach coherence times, T_2, of up to one hundred microseconds[1,2] which allows for high-fidelity gate operations and places superconducting circuits close to the error threshold required for fault-tolerant quantum computation[3–5]. However, improving coherence remains imperative in order to reduce the overhead required for fault tolerance[6] and facilitate operations with finite latency, such as encountered in protocols using measurement and digital feedback. It is a continuing challenge to engineer superconducting circuits that enable longer coherence times and, crucially, to understand the limitations on the timescales achievable.

A promising route forward is to supplement Josephson circuits with additional, highly coherent systems for quantum state storage[7]. To this end, quantum excitations have been swapped successfully between Josephson junction-based two-level systems and naturally long-lived systems, such as solid-state defects and spins[8–11]. However, no memory times exceeding those achievable with superconducting artificial atoms (such as transmons) alone have been reported for any such hybrid system yet. Achieving sufficient coupling strength for coherent quantum state transfer, without introducing new channels for decoherence, remains a substantial technical challenge.

Superconducting microwave resonators are particularly interesting for quantum state storage. For one, they are routinely integrated with superconducting circuits in what is known as circuit QED, allowing for instance the generation and manipulation of highly non-classical photonic states[12–14]. Further, the high-dimensional Hilbert space available can open up new avenues for continuous-variable quantum information processing[15–17]. Importantly, superconducting three-dimensional (3D) microwave cavities can reach very high quality factors, enabling storage times approaching seconds[18,19], even at the single-photon level[20]. Long-lived cavities that are, in principle, circuit QED compatible have been demonstrated[21]. However, cavities face new loss mechanisms when coupled to Josephson-junction circuits and typically observed coherence times are reduced by orders of magnitude[13,14]. It is thus an important question as to where these losses originate, and whether they can be eliminated in order to render cavities useful as quantum memories for circuit QED.

In this work we introduce a microwave cavity quantum memory that allows for storing quantum superpositions with millisecond relaxation and pure dephasing times. These long coherence times are enabled by a novel hardware architecture that is designed to be robust against the imperfect connection between parts of the system that arises when physically integrating the cavity with a superconducting transmon qubit. Crucially, the long-lived memory resonator is coupled strongly to a transmon, allowing for quantum control of the resonator state on the MHz-scale. We characterize the coherence of the resonator with superpositions of Fock states, finding $T_1 = 1.22 \pm 0.06\,\mathrm{ms}$ and $T_2 = 0.72 \pm 0.03\,\mathrm{ms}$, thus sustaining coherence nearly an order of magnitude longer than the best superconducting circuit previously reported[22]. Our analysis places limits on the additional loss channels present in the coupled system beyond those of the

* matthew.reagor@yale.edu

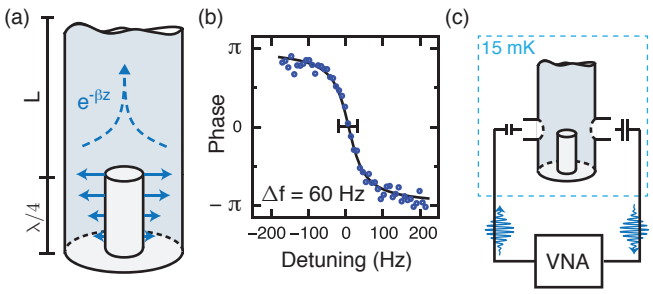

Figure 1. High-Q coaxial microwave cavity. **(a)** A quarter-wave coaxial resonator is defined by short-circuiting the inner and outer conductors of the coaxial transmission line at one location (bottom) and open-circuiting the line a distance $\lambda/4$ away (upward). Fields are suppressed exponentially in the upward direction, eliminating losses at the seam. **(b)** The measured linear response in transmission at single-photon excitation levels show typical quality factors of $Q \sim 7 \times 10^7$, corresponding to a line width of about 60 Hz. **(c)** Samples are characterized at 15 mK with a vector network analyzer (VNA).

uncoupled constituents. These findings point to future improvements of the system and have implication for various schemes of quantum information processing with harmonic oscillators.

II. HIGH-Q COAXIAL $\lambda/4$ RESONATOR

Superconducting microwave cavities can achieve low energy decay rates, $\kappa/2\pi$ = (1-100) Hz, for single microwave photons[20,21]. However, leveraging such cavities as quantum memories for circuits has remained an outstanding challenge. Combining resonators with transmons has resulted in enhanced loss rates, $\kappa/2\pi \gtrsim 1\,\mathrm{kHz}$[13,14], which can also achieved by a transmon alone. Several dissipation mechanisms are introduced alongside a superconducting qubit, including substrate loss[23], and mechanical instability. Moreover, 3D cQED systems require assembly from parts in order to allow for integration of Josephson-junction based circuits on chips. Due to finite contact resistance this practice introduces dissipative seams that have been identified as a contributor to enhanced decay rates[18,21,24].

A. Design of the Cavity Memory

The design of our high-Q coaxial $\lambda/4$ resonator is illustrated in Figure I. The inner and outer conductors of the coaxial transmission line section are formed with a continuous piece of aluminum. The transmission line is, therefore, interrupted at one end ($z = -\ell$) by a short circuit. The other end of the line ($z = 0$) is terminated in an effective open circuit, as discussed below, which establishes a resonance condition when $\ell \approx \lambda/4$.

The key element for suppressing seam dissipation is a circular waveguide of length L and high cut-off frequency, $f_c \gg f_0$. The waveguide is located between one end of coaxial transmission line ($z = 0$) a light-tight seal ($z = L$), to protect the $\lambda/4$ mode from contact resistance at that joint since fields exponentially decay in this region ($z > 0$). By its nature, the waveguide element also establishes the open circuit boundary condition of the resonator.

The resonator couples to several circular modes in the waveguide section. Of these waveguide modes, the TM_{01} mode has the lowest cutoff frequency. Therefore, the TM_{01} mode sets the $\lambda/4$ mode's propagation into the waveguide. The evanescent TM_{01} mode has a propagation constant $\beta = \sqrt{k^2 - (2.41/a)^2}$, where $k = 2\pi/\lambda$ is the wavenumber, and $a = 5\,\mathrm{mm}$ is the radius of the circular waveguide section[25]. At our transmission line's fundamental resonance frequency, the propagation constant is $\beta = \imath/2.03\,\mathrm{mm}$, below cutoff. Therefore, the $\lambda/4$ mode's energy density falls as $|E \times H| \propto e^{-2|\beta|z}$ into the waveguide section. Finite element simulations (Ansys HFSS), which take into account all possible waveguide modes, confirm these simple predictions to within 5%. We seal the cavity for light-tightness after a length of waveguide section that is $L \approx 10/|\beta|$. The resonator's energy has been suppressed at this location by a factor of about e^{-20}. We therefore rule out assembly defects such as contact resistance as a potentially limiting dissipation mechanism at internal quality factors of $Q_{\mathrm{int}} \sim 10^9$.

Cavities are fabricated from high purity (4N) aluminum[21] and driven by a pin coupler through a hole in the side wall of the cavity[1]. The mode is strongly undercoupled to avoid external damping ($\kappa_{\mathrm{ext}}/2\pi \approx 1\,\mathrm{Hz}$). All experiments are performed in a dilution refrigerator at a base temperature of about 15 mK (Fig. 1).

B. Quality Factor

In order to estimate the maximum quality of our bare coaxial transmission line memory we measure its frequency response a vector network analyzer (VNA). We use the shunt-resonator technique to separate the internal quality factor (Q_{int}) from the external coupling quality factor (Q_{ext})[26–28]. In particular, the data shown in Fig. 1a is evaluated along the frequency-parametrized complex circle that is traced out in the transmitted linear voltage (S21) in this measurement configuration as done in[26]. We determine a typical single-photon quality factor $Q = 7 \times 10^7$, corresponding to a single-photon lifetime of approximately 3 ms. This result is consistent with the material quality observed earlier for bulk aluminum[21].

The VNA measurements further allow us to place a bound on the quality of the dielectric (Q_{diel}) and conductor (Q_{mag}) surfaces for our high purity aluminum by assuming that all loss comes from either a dielectric loss

($Q_{\rm int} \propto Q_{\rm diel}$) or conductor loss ($Q_{\rm int} \propto Q_{\rm mag}$). By finite element simulations we calculate the normalized field-energy stored in the surface layer of our cavity. These calculations allow us to estimate the participation ratios[29,30] for the AlO_x dielectric of $p_{\rm diel} = 2 \times 10^{-7}$ (assuming an oxide thickness of 3 nm and a relative dielectric constant of 10), and a kinetic inductance fraction[31], or magnetic participation ratio, of $p_{\rm mag}= 4{\times}10^{-5}$ (using a penetration depth of 50 nm[21]). These measurements thus achieve a bound for bulk, high purity aluminum of $Q_{\rm diel} \geq 14$ and $Q_{\rm mag} \geq 3000$ at single-photon levels.

At large circulating field strengths, corresponding to millions of photons in the resonator, we find higher quality factors, $Q_{\rm int} = 2 \times 10^8$, corresponding to a lifetime of 7 ms. The saturable nature of this dominate loss mechanism indicates that material defects[30,32–34] are a limiting factor for this particular cavity as a memory.

III. ADDING A TRANSMON

In addition to the high quality factors achievable, the small mode volume makes this quarter-wave resonator particularly attractive for integration with transmon qubits. By inserting a sapphire chip holding the transmon as shown in Fig. 2, we can align the dipole moment of the transmon with the electric field polarization, and are able to achieve strong coupling between the transmon and the memory resonator. The location, orientation, and size of the antenna pads of the transmon sets the strength of coupling to the cavity. The transmon is further coupled to a second, strongly overcoupled cavity with $\omega_r/2\pi = 9.8$ GHz that is used for measuring the transmon state.

Fig. 2b shows schematically the experimental setup used to characterize the combined transmon/memory system. Similarly to the previously described input coupling of the storage cavity, transmon and readout resonator drives are applied capacitively through a pin that couples to the readout cavity. To measure the transmon state we measure the state dependent transmission through the readout resonator. We amplify the signal with a Josephson parametric converter[35] (JPC) at base temperature, and demodulate and digitize the signal using an FPGA system with home-built software at room temperature to obtain measurement outcomes.

A. Transmon Fabrication and Properties

The transmon circuit is fabricated on a 430 μm thick sapphire wafer with a Niemeyer-Dolan bridge process. A bilayer of resists (MMA/PMMA) support a suspended structure at the Josephson tunnel junction location and are completely stripped where the antenna is to be deposited. Both exposures are completed in a single step of electron-beam lithography. Before deposition, the sapphire surface is cleaned with Ar/O_2 ion etching. We

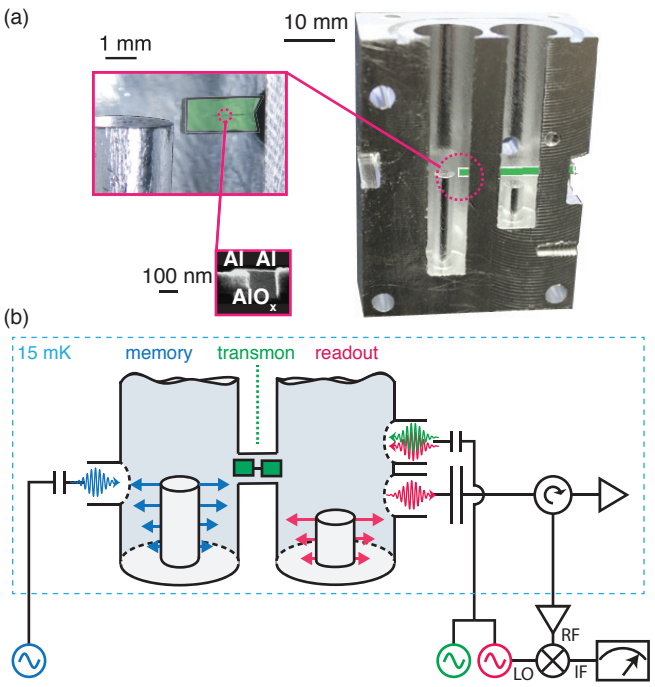

Figure 2. Quantum memory and experiment scheme. To realize a quantum memory, a superconducting transmon qubit on sapphire (green) is inserted through small hole. **(a)** False-colored image showing a cross-section of the system, with insets that show the transmon chip and a micrograph of the junction. **(b)** Schematic of the experiment. The transmon is coupled to the memory cavity as well as a second cavity used for readout. Weakly coupled pins are used for input signals (depicted as small capacitors). The measurement signal is extracted via a pin coupled strongly to the readout resonator (large capacitor) and amplified by a Josephson parametric converter (JPC) at base temperature of the dilution refrigerator, and subsequently demodulated using the readout oscillator (LO) as reference.

deposit aluminum with double-angle evaporation ($\pm 28°$) with thicknesses of 20 nm and 60 nm, exposing the chamber to oxygen in between these depositions (720 seconds in 2000 Pa static pressure of a gaseous mixture of 85% argon and 15% oxygen) and again before removing the sample (600 seconds, 400 Pa). After liftoff, the transmon junction has a normal-state resistance of 3.5 kΩ at room temperature, corresponding to a Josephson inductance of $L_{\rm J} = 4.5$ nH, or a Josephson energy of $E_{\rm J} = \Phi_0^2/((2\pi)^2\hbar L_{\rm J}) = 150\,\mu$eV at 15 mK. The transmon dipole antenna pads are approximately 2 mm long to achieve strong coupling to both resonators and 50 μm wide to maintain a large anharmonicity.

The fabrication parameters result, after packaging the chip as shown in Fig. 2, in a transition frequency from the ground state $|g\rangle$ to the first excited state $|e\rangle$ of $\omega_{\rm t}/2\pi \equiv \omega_{\rm eg}/2\pi = 7.9$ GHz, and an anharmonicity of $\alpha/2\pi \equiv (\omega_{\rm ef} - \omega_{\rm ge})/2\pi = -146$ MHz. For the transmon relaxation and coherence times, we find $T_{1,t} = 15\,\mu$s and

$T_{2,t} = 10\,\mu$s.

B. System Hamiltonian

In this system, two cavities are coupled to the transmon in the strong dispersive regime of cavity QED, resulting in the combined system Hamiltonian[13]

$$\begin{aligned}\frac{H}{\hbar} =\ & \omega_{\rm s}\hat{a}_{\rm s}^\dagger\hat{a}_{\rm s} + \omega_{\rm t}\hat{a}_{\rm t}^\dagger\hat{a}_{\rm t} + \omega_{\rm r}\hat{a}_{\rm r}^\dagger\hat{a}_{\rm r} \\ & + \chi_{\rm sq}\hat{a}_{\rm s}^\dagger\hat{a}_{\rm s}\hat{a}_{\rm t}^\dagger\hat{a}_{\rm t} + \chi_{\rm rt}\hat{a}_{\rm r}^\dagger\hat{a}_{\rm r}\hat{a}_{\rm t}^\dagger\hat{a}_{\rm t} \\ & + \frac{K_{\rm s}}{2}\hat{a}_{\rm s}^{\dagger 2}\hat{a}_{\rm s}^2 + \frac{\alpha}{2}\hat{a}_{\rm t}^{\dagger 2}\hat{a}_{\rm t}^2 + \frac{K_{\rm r}}{2}\hat{a}_{\rm r}^{\dagger 2}\hat{a}_{\rm r}^2,\end{aligned} \tag{1}$$

where indices s, t, and r represent storage, transmon, and readout respectively. $\hat{a}_i$ is the annihilation operator and K_i the self-Kerr interaction (i.e., anharmonicity) of mode i, respectively, and χ_{ij} is the cross-Kerr interaction between modes i and j. We have neglected the interaction between the two cavities as well as higher order terms, all of which can be expected to be small[36]. The simulated and measured Hamiltonian values for this device are presented in Table I.

Table I. Predicted and extracted parameters for the full device device Hamiltonian (Eq. 1).

$H/\hbar$	Experiment (Hz)	Simulation (Hz)	Deviation (%)
$\omega_s/2\pi$	4.250 $\times 10^9$	4.246 $\times 10^9$	< 1
$\omega_q/2\pi$	7.906 $\times 10^9$	7.878 $\times 10^9$	< 1
$\omega_r/2\pi$	9.777 $\times 10^9$	9.653 $\times 10^9$	1
$\chi_{sq}/2\pi$	- 4.99 $\times 10^5$	- 5.56 $\times 10^5$	11
$\chi_{rq}/2\pi$	- 8.25 $\times 10^5$	- 7.77 $\times 10^5$	6
$\chi_{sr}/2\pi$	-	- 1.60 $\times 10^3$	-
$K_s/2\pi$	- 4.50 $\times 10^2$	- 5.20 $\times 10^2$	16
$\alpha/2\pi$	- 1.46 $\times 10^8$	- 1.41 $\times 10^8$	3
$K_r/2\pi$	-	- 1.20 $\times 10^3$	-

For the following characterizing of the memory, we adopt the simplified Hamiltonian

$$\hat{H}_{\rm int}/\hbar = \frac{\chi}{2}\hat{a_s}^\dagger\hat{a_s}\hat{\sigma}_z, \tag{2}$$

where we have truncated the transmon Hilbert space to its first two levels to describe it with the Pauli operator $\hat{\sigma}_z$ and made a transformation into the rotating frames of both transmon and cavity.

The hallmark of this strong dispersive coupling is revealed in spectroscopy by the fact that the cavity resonance frequency depends on the transmon state, and vice versa (Fig. 3a). From the splitting we obtain $\chi/2\pi = -0.5$ MHz, meaning that operations on the cavity can be performed on time scales of $\sim 1\,\mu$s. This value of χ further indicates that the anharmonicity of the cavity mode is small, on the order of $K_s/2\pi \approx 500$ Hz (Table I).

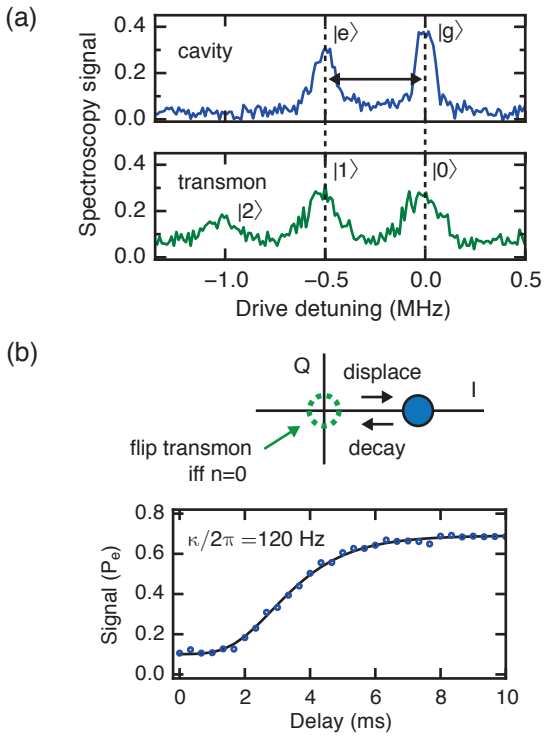

Figure 3. Initial characterization of the cavity-transmon system. **(a)** With strong dispersive coupling, the spectrum of the resonator depends on the state of the transmon (top) and vice versa (bottom). **(b) (top)** The decay rate of the resonator can be measured by monitoring the population of the vacuum state after displacing the resonator; the state is schematically represented as a blue circle in the IQ plane of the resonator. **(bottom)** From the population decay we extract a decay rate of $\kappa/2\pi = 120 \pm 5$ Hz, see main text for details.

Utilizing the dispersive coupling to the transmon, we can efficiently determine the energy decay rate of the cavity κ at the single-photon level (Fig. 3b). We first displace the resonator to create a coherent state with $\beta_0 = \sqrt{\bar{n}} = 3$, where β_0 is the independently calibrated displacement amplitude and $\bar{n}$ is the mean number of photons. This state decays as $\beta(t) = \beta_0 \exp(-\kappa t/2)$, and the probability to find the cavity in its vacuum state is $P_{\rm vac}(t) = \exp(-|\beta(t)|^2)$. We probe the vacuum population directly by applying a narrow-bandwidth (FWHM $\ll \chi/2\pi$) photon number-selective π-pulse on the transmon, centered on the $|g,0\rangle \rightarrow |e,0\rangle$ transition. This pulse is immediately followed by a measurement of the transmon state. The probability for the transmon to be measured in the excited state is $P_{\rm e}(t) \propto \exp\left(-|\beta_0|^2\exp(-\kappa t)\right)$. By fitting the decay curve (Fig. 2b) we extract $\kappa/2\pi = 120 \pm 5$ Hz, corresponding to a quality factor of $Q = 3.5 \pm 0.1 \times 10^7$ and a life time of $T_{\rm cav} = 1/\kappa = 1.33 \pm 0.06$ ms. This constitutes only a fairly small increase in energy relaxation induced by the circuit integration, since the extracted Q is comparable to the linear measurements reported in

Section II. Importantly, this lifetime exceeds that of the transmon by almost two orders of magnitude, while they are still coupled strongly.

IV. QUANTUM MEMORY CHARACTERIZATION

A. Relaxation and Dephasing

For evaluating the resonator as a quantum memory it is essential to quantify its coherence time, T_2, by the decay of quantum states. The coherence time is bounded by the relaxation time, $T_1 = 1/\kappa$, as $1/T_2 = 1/(2T_1) + 1/T_\phi$. Analogously to the case of a two-level system, the pure dephasing time (transversal relaxation time), T_ϕ, is the time constant with which the coherence between a pair of Fock states, n and $n+1$, decays in the absence of energy relaxation (longitudinal relaxation). T_1, T_2 can be measured directly by monitoring the time evolution of the resonator after generating the Fock state $|1\rangle$ or the superposition state $(|0\rangle + |1\rangle)/\sqrt{2}$, respectively.

In our cQED system, arbitrary Fock states and their superpositions can be generated in the resonator by a combination of appropriately chosen cavity mode displacements and number-state selective phase gates on the transmon, following the prescription from Heeres, *et al.*[37] (Fig. 4a). To generate $|1\rangle$, we first displace the resonator to $\beta = 1.14$ via a short pulse with Gaussian envelope. Subsequently we apply a 2π rotation on the transmon that is selective on the zero-photon peak, driving the transition $|g,0\rangle \rightarrow |e,0\rangle$, thus applying a phase only on the vacuum Fock state. A final displacement of $\beta = -0.56$ completes the Fock-state creation. The superposition of $(|0\rangle + |1\rangle)/\sqrt{2}$ is generated by a slightly modified pulse sequence, using displacements $\beta = \{0.56, -0.24\}$ interleaved again with a selective 2π rotation on the transmon. In a dissipationless system, this sequence will deterministically create the desired state with 99% fidelity[38]. Finite transmon coherence limits our quality of state preparation (Fig. 4b) which does, however, not impact our coherence measurements as they rely only on a population difference.

After preparing the state $|1\rangle$ we measure the time-dependent probability for finding the resonator in the vacuum, yielding $T_1 = 1.22 \pm 0.06$ ms, in agreement with the classical energy decay rate extracted from coherent states (Fig. 5a). To find the coherence time T_2 of the resonator, we prepare the mode in the state $(|0\rangle + |1\rangle)/\sqrt{2}$ and measure the decay of coherence between $|0\rangle$ and $|1\rangle$ (Fig. 5b). This is done in close analogy to Ramsey-type measurements done for two-level systems or resonators: we reveal the coherent phase between these two states with a third displacement pulse on the cavity (taking the role of a $\pi/2$ pulse in a two-level system experiment), with displacement amplitude $\beta = 0.8e^{j\omega t}$, where ω is a small detuning. Measuring the probability to find the resonator in the vacuum then yields a detected signal

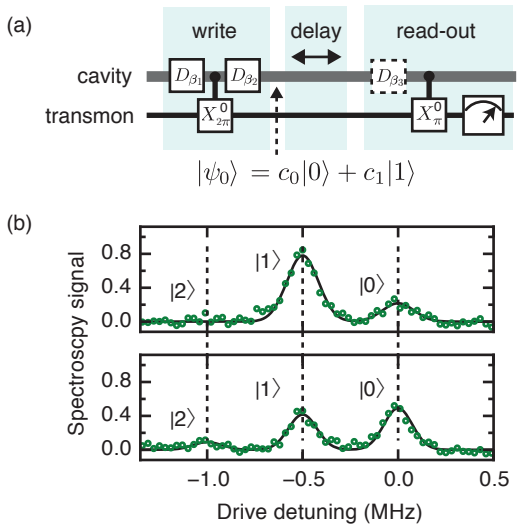

Figure 4. Preparation of quantum resonator states. **(a)** Arbitrary Fock state superpositions can be written to the cavity memory using a series of displacements on the cavity and number-selective phase gates on the transmon. **(b)** To verify the input states for the resonator's T_1, T_2 experiments, we perform spectroscopy on the transmon after preparing the resonator in an input state. **(top)** When the cavity is mostly in the first Fock state, $|1\rangle$, the transmon's frequency distribution reflects these statistics. By the normalized area under each peak, we determine that the population of each Fock state (P_n) is $P_0 = 0.21 \pm 0.02$, $P_1 = 0.75 \pm 0.02$, $P_2 = 0.04 \pm 0.02$ **(bottom)** After preparing a superposition of $|0\rangle$ and $|1\rangle$, we find the distribution to be $P_0 = 0.49 \pm 0.02$, $P_1 = 0.41 \pm 0.02$, $P_2 = 0.10 \pm 0.02$. This experiment alone is not sufficient to distinguish between a statistical mixture of these states and a coherent superposition. However, the phase coherence is revealed in the sinusoidal oscillations of the subsequent T_2 experiment.

proportional to the state's phase coherence. The decay of the measured signal yields $T_2 = 0.72 \pm 0.03$ ms or a pure dephasing time $T_\phi = 0.98 \pm 0.05$ ms. Importantly, coherence persists significantly longer than reported for any previous superconducting quantum circuit architecture so far ($T_2 \leq 0.095$ ms)[2], showing clearly the suitability of the cavity for serving as a quantum memory.

B. Coherence-limiting Mechanisms

It is critical for our understanding of the cavity memory to identify decoherence mechanisms that are introduced together with the coupling to the transmon. We expect that photon-loss in the resonator should be affected by the dissipation of the transmon as consequence of the hybridization between the modes. This is analogous to the 'bad-cavity' limit of cavity QED, where an atom's emission is enhanced by Purcell coupling to a low-Q cavity[39]. In our case the cavity is longer lived than the

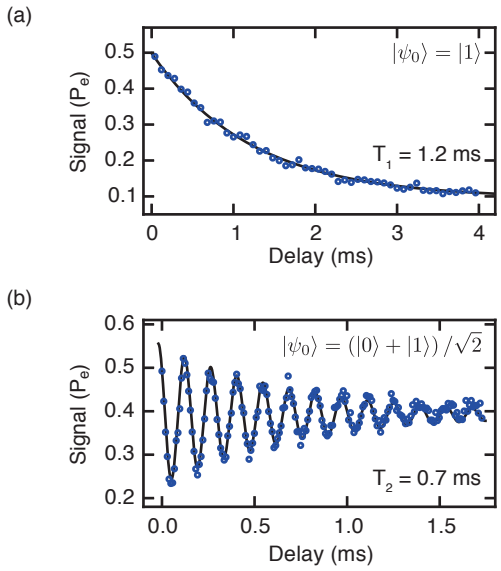

Figure 5. Coherence of the quantum memory. **(b)** To prepare the Fock state $|1\rangle$, the optimal choice of displacements is $\beta_1 = 1.14$ and $\beta_2 = -0.58$[37]. A single-photon decay lifetime of $T_1 = 1.22 \pm 0.06$ ms is extracted from the decay of the state. **(c)** A superposition of the Fock states $|0\rangle$ and $|1\rangle$ is created with $\beta_1 = 0.56$ and $\beta_2 = -0.24$. A final displacement of $\beta_1 = 0.8\exp(j\omega t)$ is used to measure the coherence of the superposition. This Ramsey-like experiment yields $T_2 = 0.72 \pm 0.03$ ms from which we infer $T_\phi \approx 1$ ms.

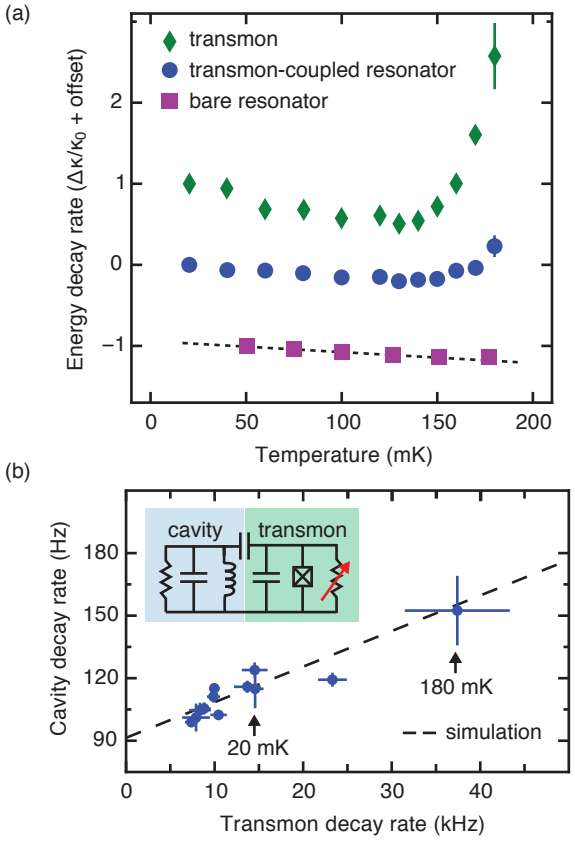

Figure 6. Transmon-induced dissipation. The resonator inheritd a photon-loss channel from coupling to the lossy transmon qubit. This effect can be revealed by tuning the decay rates *in situ*. **a** We monitor the decay rates of the transmon (green diamonds), transmon-coupled memory resonator (blue circles), and an empty resonator (purple squares) as a function of temperature. We present the relative change in those decay rates, offset to aide visualization. Decreases in the decay rates (improvements in lifetime) are observed for all three modes at elevated temperatures below 150 mK. The dashed line is a best linear fit to the bare resonator's temperature dependence in this range. Above 150 mK, the quasiparticle sensitivity of the transmon causes at a sharp increase in the decay rate for both the transmon and the transmon-coupled resonator, while the bare resonator continues its trend toward improvement. **b** Parameterized version of the above, with the transmon-coupled resonator decay rates shown against the transmon decay rates. The observed correlation agrees with the predicted transmon-induced loss channel from a three-dimensional electromagnetic simulation of the device.

artificial atom, leading to an 'inverse Purcell effect'. A simple cavity QED treatment[40] would suggest that the resonator mode inherits an additional decay rate from the transmon, $\kappa_q \approx (g^2/\Delta^2) \times \gamma$, due to the mode hybridization, where g is the vacuum Rabi rate, Δ is the detuning, and γ the decay rate of the transmon mode.

For a quantitative analysis we perform a numerical finite element simulation of our system, predicting an enhancement of $\kappa_q \approx \gamma/600$. In an eigenmode-type solver (HFSS) we add a parallel shunt resistor to the linear inductor that represents the Josephson junction in simulation. The only loss in the calculation arises from currents passing through the inductor. Thus, the ratio of the resulting quality factors is expected to be the scaling between an otherwise perfect cavity's lifetime and the lifetime of the imperfect transmon.

We can experimentally test this model even without *in situ* control over g or Δ. Instead, we study the relationship between γ and κ directly by varying the amount of quasiparticle loss in the system, which is controlled by regulating its physical temperature. Although all modes in the system will have more loss at elevated temperatures, the transmon mode has the highest kinetic inductance fraction[41] and is, therefore, the most sensitive to quasiparticle loss. More precisely, we can express the total decay rate of the transmon-coupled resonator as

$$\kappa_{\rm tot}(T) = \kappa_{\rm q}(T) + \kappa_0(T), \qquad (3)$$

where κ_q is the transmon-induced decay rate, and κ_0 is the bare resonator decay rate. Because κ_q is strongly temperature dependent, the inverse Purcell effect should manifest itself in an enhanced quasiparticle-sensitivity for the resonator. Indeed, we observe this distinct trend

while monitoring the decay rates at temperatures up to 180 mK (Fig. 6a).

To quantify the inverse Purcell loss channel, we measured the decay rate of the transmon-coupled resonator $\kappa_{\rm tot}(T)$ using techniques shown in Fig. 3b and also monitored the decay rate of the transmon γ at each temperature. We controlled for the behavior of the bare resonator ($\kappa_0(T)$)) by performed temperature dependent Q measurements on an empty resonator (Fig. 6a). The linear cavity shows a slight trend toward increased lifetime at elevated temperatures below 180 mK, up to 15%. We use the best fit linear trend (dashed line Fig. 6a) as $\delta\kappa_0(T)$). However, we note that this small effect changes the subsequent analysis by only 2% as compared to a model where κ_0 is a constant.

In Figure 6b, we correlate the transmon's decay rate to transmon-coupled resonator decay rate for all recorded temperatures. The linear scaling between the two rates ($\kappa_{\rm q} = (650 \pm 200)^{-1}\gamma$) is in quantitative agreement with the prediction from the simulation. This analysis also yields an intrinsic resonator lifetime, $1/\kappa_0 = 2\,$ms, consistent with measurements on empty cavities. This finding suggests that any enhancement in the energy decay rate of the resonator originates from the coupling alone, and is not caused by new, unknown channels that are introduced by the methods used to physically assemble the joint transmon-cavity system.

We observe a finite pure dephasing time for the resonator state, such that $T_2 < 2T_1$. This means that energy decay is not the only source of decoherence in the resonator, with serious implications for quantum error correction schemes that only assume photon loss[17]. It has been shown that photon shot noise inside a resonator leads to enhanced qubit dephasing in cQED[2,42]. We now show that applying this model to the thermal excited state population of the transmon[43] can also explain the observed excess dephasing of cavity states. The key observation is that this dephasing mechanism is symmetric: if one mode undergoes a stochastic photon number jump, it changes the other mode's frequency by χ, leading to rapid loss of phase information whenever the uncertainty in the time of a stochastic jump is greater than $1/\chi$. The cavity dephasing rate is then given by the transmon jump rate as $\Gamma_\phi \approx P_{\rm e}\gamma$, where $P_{\rm e}$ is the excited state population of the transmon.

An exact model for the pure-dephasing of a transmon due to thermal photons in strongly coupled, lossy resonators has been developed for the dispersive regime of cQED in which we operate[2,44]. However, because our Hamiltonian is symmetric, this model is directly applicable to resonators being subjected to the reverse process of thermal shot-noise in the transmon mode. The dephasing rate Γ_ϕ derived in[2,44], can thus be used for our case of a resonator coupled to a single, thermally populated transmon as

$$\Gamma_\phi = \frac{\gamma}{2}{\rm Re}\left[\sqrt{\left(1+\frac{2\imath\chi}{\gamma}\right)^2+\frac{8\imath\chi P_e}{\gamma}}-1\right], \qquad (4)$$

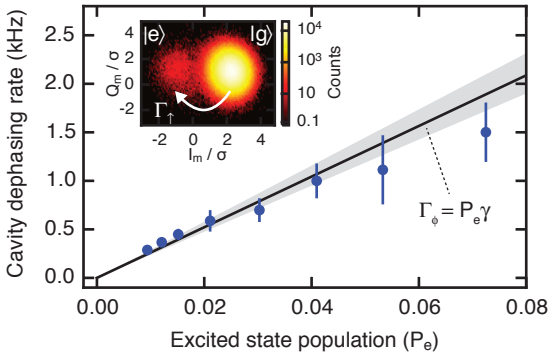

Figure 7. Transmon-induced dephasing. **(inset)** A histogram of single-shot measurements of the transmon state, taken in equilibrium with a parametric amplifier, reveals a finite population in the transmon $|e\rangle$ state of $P_e = 0.8\%$. In the histogram, the measurement records, $\{I_m, Q_m\}$, from the homodyne detection have been scaled by the vacuum fluctuation amplitude, σ. Quantum jumps due to this thermal bath, $\Gamma_\uparrow$, will dephase the state in the cavity memory at rate $P_e\kappa_q$. **(main)** The dephasing rate of the cavity memory Γ_ϕ is measured while the transmon is excited weakly via a resonant drive. The observed total cavity dephasing rate, as a function of P_e, is in agreement with a model that assumes no intrinsic dephasing in the cavity. Error bounds have been determined using bootstrapping.

where P_e is the excited state population of the transmon and γ is the transmon's decay rate. Expanding this expression in the strong dispersive limit ($\chi \gg \gamma$) gives

$$\Gamma_\phi \approx P_e\gamma\left[1-\mathcal{O}\left(\frac{\gamma}{\chi}\right)^2\right]. \qquad (5)$$

The quadratic term is of order 1×10^{-4} and thus neglected in our analysis.

We extract $P_{\rm e}$ for the transmon by performing repeated single shot measurements on the sample (Fig. 4b, inset), finding $P_{\rm e} = 0.8\%$, an effective temperature of 80 mK. In order to test the dependence of Γ_ϕ on P_e, we monitor the T_2 of the resonator while applying weak drives on the transmon to populate $|e\rangle$, creating a known increase in the jump rate. The total dephasing of the cavity should be given by $\Gamma_\phi = P_{\rm e}\gamma + \Gamma_\phi^0$, where Γ_ϕ^0 is the intrinsic dephasing of the resonator. We find that, to the precision of our measurement, the observed T_2 decays can be entirely explained by the calibrated $P_{\rm e}$ and observed γ (the theory line in Fig. 4b), consistent with the resonator having negligible intrinsic dephasing mechanisms ($\Gamma_\phi^0/2\pi \lesssim 40\,$Hz). An encouraging conclusion from these results is therefore that appropriate remedies against thermal population, such as improved thermalization[45–47], could extend the coherence of this quantum memory back to $2T_1$, leaving photon loss as the only source of decoherence.

V. CONCLUSION AND OUTLOOK

We have demonstrated a long-lived superconducting cavity resonator that can serve as a useful quantum memory for superconducting quantum circuits, as it enhances the available coherence beyond what can be achieved with the best available transmons alone. An important conclusion from our data is that all of the observed decoherence can be accounted for by the bare resonator quality factors ($Q \approx 5 \times 10^7$), the coupling Hamiltonian, and the transmon properties alone. Unlike earlier quantum memories for superconducting circuits, including cavities, our system shows no further, unknown decoherence channels that arise from connecting the individual constituents. We emphasize that therefore, with given properties of the cavity and the transmon as well as the coupling Hamiltonian, the coherence properties of the memory are optimal, and can only be improved by employing better transmons or cavities. It can be expected that this observation of the coupling induced decoherence will be useful for ongoing efforts to harness hybrid quantum systems for enhancing the coherence times in superconducting circuits[7].

Because our device reaches the strong dispersive regime of cavity QED, control and measurement can be conducted on fast timescales set by $t = \pi/\chi$. The resonator presented shows little degradation on this timescale, with $\chi T_1 \approx 3000$, suggesting that quantum operations with very high fidelities can be performed, and that error syndromes on quantum states encoded in microwave photons can be detected much more rapidly than errors occur. The architecture shown can serve as an ideal platform for quantum information processing with resonator states and we expect that it will enable further advancement towards fault tolerance in superconducting quantum computing.

ACKNOWLEDGEMENTS

We thank B. Vlastakis, G. Kirchmair, U. Vool, Z. Leghtas, D. Schuster, and H. Paik for helpful discussions. Facilities use was supported by YINQE and NSF MRSEC DMR 119826. This research was supported by ARO under Grant No. W911NF-14-1-0011. W.P. was supported by NSF grant PHY1309996 and by a fellowship instituted with a Max Planck Research Award from the Alexander von Humboldt Foundation.

[1] H. Paik, D. I. Schuster, L. S. Bishop, G. Kirchmair, G. Catelani, A. P. Sears, B. R. Johnson, M. J. Reagor, L. Frunzio, L. I. Glazman, S. M. Girvin, M. H. Devoret, and R. J. Schoelkopf, Physical Review Letters **107**, 240501 (2011).

[2] C. Rigetti, J. M. Gambetta, S. Poletto, B. L. T. Plourde, J. M. Chow, A. D. Corcoles, J. A. Smolin, S. T. Merkel, J. R. Rozen, G. A. Keefe, M. B. Rothwell, M. B. Ketchen, and M. Steffen, Physical Review B **86**, 100506 (2012).

[3] R. Barends, J. Kelly, A. Megrant, A. Veitia, D. Sank, E. Jeffrey, T. C. White, J. Mutus, A. G. Fowler, B. Campbell, Y. Chen, Z. Chen, B. Chiaro, A. Dunsworth, C. Neill, P. O'Malley, P. Roushan, A. Vainsencher, J. Wenner, A. N. Korotkov, A. N. Cleland, and J. M. Martinis, Nature **508**, 500 (2014).

[4] D. Risté, S. Poletto, M. Z. Huang, A. Bruno, V. Vesterinen, O. P. Saira, and L. DiCarlo, Nature Communications **6**, 6983 (2015).

[5] A. D. Córcoles, E. Magesan, S. J. Srinivasan, A. W. Cross, M. Steffen, J. M. Gambetta, and J. M. Chow, Nature Communications **6**, 6979 (2015).

[6] B. M. Terhal, Reviews of Modern Physics **87**, 307 (2015).

[7] G. Kurizki, P. Bertet, Y. Kubo, K. Mølmer, D. Petrosyan, P. Rabl, and J. Schmiedmayer, Proceedings of the National Academy of Sciences **112**, 3866 (2015).

[8] M. Neeley, M. Ansmann, R. C. Bialczak, M. Hofheinz, N. Katz, E. Lucero, A. O/'Connell, H. Wang, A. N. Cleland, and J. M. Martinis, Nature Physics **4**, 523 (2008).

[9] X. Zhu, S. Saito, A. Kemp, K. Kakuyanagi, S.-I. Karimoto, H. Nakano, W. J. Munro, Y. Tokura, M. S. Everitt, K. Nemoto, M. Kasu, N. Mizuochi, and K. Semba, Nature **478**, 221 (2011).

[10] Y. Kubo, C. Grezes, A. Dewes, T. Umeda, J. Isoya, H. Sumiya, N. Morishita, H. Abe, S. Onoda, T. Ohshima, V. Jacques, A. Dreau, J. F. Roch, I. Diniz, A. Auffeves, D. Vion, D. Esteve, and P. Bertet, Physical Review Letters **107**, 220501 (2011).

[11] Y. Tabuchi, S. Ishino, A. Noguchi, T. Ishikawa, R. Yamazaki, K. Usami, and Y. Nakamura, Science **349**, 405 (2015).

[12] M. Hofheinz, H. Wang, M. Ansmann, R. C. Bialczak, E. Lucero, M. Neeley, A. D. O'Connell, D. Sank, J. Wenner, J. M. Martinis, and A. N. Cleland, Nature **459**, 546 (2009).

[13] G. Kirchmair, B. Vlastakis, Z. Leghtas, S. E. Nigg, H. Paik, E. Ginossar, M. Mirrahimi, L. Frupzio, S. M. Girvin, and R. J. Schoelkopf, Nature **495**, 205 (2013).

[14] L. Bretheau, P. Campagne-Ibarcq, E. Flurin, F. Mallet, and B. Huard, Science **348**, 776 (2015).

[15] D. Gottesman, A. Kitaev, and J. Preskill, Phys. Rev. A **64**, 012310 (2001).

[16] S. L. Braunstein and P. van Loock, Rev. Mod. Phys. **77**, 513 (2005).

[17] M. Mirrahimi, Z. Leghtas, V. V. Albert, S. Touzard, R. J. Schoelkopf, L. Jiang, and M. H. Devoret, New Journal of Physics **16**, 045014 (2014).

[18] J. P. Turneaure and N. T. Viet, Applied Physics Letters **16**, 333 (1970).

[19] H. Padamsee, Superconductor Science and Technology **14**, R28 (2001).

[20] S. Kuhr, S. Gleyzes, C. Guerlin, J. Bernu, U. B. Hoff, S. Deleglise, S. Osnaghi, M. Brune, J. M. Raimond, S. Haroche, E. Jacques, P. Bosland, and B. Visentin, Applied Physics Letters **90**, 164101 (2007).

[21] M. Reagor, H. Paik, G. Catelani, L. Sun, C. Axline, E. Holland, I. M. Pop, N. A. Masluk, T. Brecht, L. Frunzio, M. H. Devoret, L. Glazman, and R. J. Schoelkopf, Applied Physics Letters **102**, 192604 (2013).

[22] We note that since the original submission of this work, results on samples with even longer lifetimes than presented here have been made available: Wang *et al.*, Science, **352**, 1087 (2016); Axline et al, arXiv:1604.06514.

[23] A. D. O'Connell, M. Ansmann, R. C. Bialczak, M. Hofheinz, N. Katz, E. Lucero, C. McKenney, M. Neeley, H. Wang, E. M. Weig, A. N. Cleland, and J. M. Martinis, Applied Physics Letters **92**, 112903 (2008).

[24] T. Brecht, M. Reagor, Y. Chu, W. Pfaff, C. Wang, L. Frunzio, M. H. Devoret, and R. J. Schoelkopf, Applied Physics Letters **107**, 192603 (2015).

[25] D. M. Pozar, *Microwave Engineering, 3rd Ed.* (John Wiley & Sons Inc, 1998).

[26] P. J. Petersan and S. M. Anlage, Journal of Applied Physics **84**, 3392 (1998), cond-mat/9805365.

[27] M. S. Khalil, M. J. A. Stoutimore, F. C. Wellstood, and K. D. Osborn, Journal of Applied Physics **111**, 054510 (2012).

[28] K. Geerlings, S. Shankar, E. Edwards, L. Frunzio, R. J. Schoelkopf, and M. H. Devoret, Applied Physics Letters **100**, 192601 (2012).

[29] J. Gao, M. Daal, A. Vayonakis, S. Kumar, J. Zmuidzinas, B. Sadoulet, B. A. Mazin, P. K. Day, and H. G. Leduc, Applied Physics Letters **92**, 152505 (2008).

[30] J. Wenner, R. Barends, R. C. Bialczak, Y. Chen, J. Kelly, E. Lucero, M. Mariantoni, A. Megrant, P. J. J. O'Malley, D. Sank, A. Vainsencher, H. Wang, T. C. White, Y. Yin, J. Zhao, A. N. Cleland, and J. M. Martinis, Applied Physics Letters **99** (2011).

[31] P. K. Day, H. G. LeDuc, B. A. Mazin, A. Vayonakis, and J. Zmuidzinas, Nature **425**, 817 (2003).

[32] J. M. Sage, V. Bolkhovsky, W. D. Oliver, B. Turek, and P. B. Welander, Journal of Applied Physics **109** (2011).

[33] A. Megrant, C. Neill, R. Barends, B. Chiaro, Y. Chen, L. Feigl, J. Kelly, E. Lucero, M. Mariantoni, P. J. J. O'Malley, D. Sank, A. Vainsencher, J. Wenner, T. C. White, Y. Yin, J. Zhao, C. J. Palmstrøm, J. M. Martinis, and A. N. Cleland, Applied Physics Letters **100** (2012).

[34] A. Bruno, G. de Lange, S. Asaad, K. L. van der Enden, N. K. Langford, and L. DiCarlo, Applied Physics Letters **106**, 182601 (2015).

[35] N. Bergeal, F. Schackert, M. Metcalfe, R. Vijay, V. E. Manucharyan, L. Frunzio, D. E. Prober, R. J. Schoelkopf, S. M. Girvin, and M. H. Devoret, Nature (London) **465**, 64 (2010).

[36] S. E. Nigg, H. Paik, B. Vlastakis, G. Kirchmair, S. Shankar, L. Frunzio, M. H. Devoret, R. J. Schoelkopf, and S. M. Girvin, Phys. Rev. Lett. **108**, 240502 (2012).

[37] R. W. Heeres, B. Vlastakis, E. Holland, S. Krastanov, V. V. Albert, L. Frunzio, L. Jiang, and R. J. Schoelkopf, Physical Review Letters **115**, 137002 (2015).

[38] S. Krastanov, V. V. Albert, C. Shen, C.-L. Zou, R. W. Heeres, B. Vlastakis, R. J. Schoelkopf, and L. Jiang, Phys. Rev. A **92**, 040303 (2015).

[39] E. M. Purcell, Physical Review **69**, 681 (1946).

[40] H. J. Kimble, Physica Scripta **1998**, 127 (1998).

[41] M. Lenander, H. Wang, R. C. Bialczak, E. Lucero, M. Mariantoni, M. Neeley, A. D. O'Connell, D. Sank, M. Weides, J. Wenner, T. Yamamoto, Y. Yin, J. Zhao, A. N. Cleland, and J. M. Martinis, Physical Review B **84**, 024501 (2011).

[42] A. P. Sears, A. Petrenko, G. Catelani, L. Sun, H. Paik, G. Kirchmair, L. Frunzio, L. I. Glazman, S. M. Girvin, and R. J. Schoelkopf, Physical Review B **86**, 180504 (2012).

[43] D. Risté, C. C. Bultink, K. W. Lehnert, and L. DiCarlo, Physical Review Letters **77**, 240502 (2012).

[44] A. A. Clerk and D. W. Utami, Phys. Rev. A **75**, 042302 (2007).

[45] R. Barends, J. Wenner, M. Lenander, Y. Chen, R. C. Bialczak, J. Kelly, E. Lucero, P. O'Malley, M. Mariantoni, D. Sank, H. Wang, T. C. White, Y. Yin, J. Zhao, A. N. Cleland, J. M. Martinis, and J. J. A. Baselmans, Applied Physics Letters **99**, 113507 (2011).

[46] A. D. Córcoles, J. M. Chow, J. M. Gambetta, C. Rigetti, J. R. Rozen, G. A. Keefe, M. B. Rothwell, M. B. Ketchen, and M. Steffen, Applied Physics Letters **99**, 181906 (2011).

[47] X. Y. Jin, A. Kamal, A. P. Sears, T. Gudmundsen, D. Hover, J. Miloshi, R. Slattery, F. Yan, J. Yoder, T. P. Orlando, S. Gustavsson, and W. D. Oliver, Physical Review Letters **114**, 240501 (2015).